



Article

# Performance Analysis of Embedded Mechanoluminescence-Perovskite Self-Powered Pressure Sensor for Structural Health Monitoring

Lucas Braga Carani , Vincent Obiozo Eze, Chetanna Iwuagwu and Okenwa Izeji Okoli \*

High-Performance Materials Institute, College of Engineering, Florida A&M University–Florida State University, 2525 Pottsdamer Street, Tallahassee, FL 32310, USA; lb15k@my.fsu.edu (L.B.C.); veze@fsu.edu (V.O.E.); chetanna1.iwuagwu@fam.u.edu (C.I.)

\* Correspondence: okoli@eng.famu.fsu.edu

Received: 31 October 2020; Accepted: 10 December 2020; Published: 18 December 2020



**Abstract:** Recent developments in sensing technologies have triggered a lot of research interest in exploring novel self-powered, inexpensive, compact and flexible pressure sensors with the potential for structural health monitoring (SHM) applications. Herein, we assessed the performance of an embedded mechanoluminescent (ML) and perovskite pressure sensor that integrates the physical principles of mechanoluminescence and perovskite materials. For a continuous in-situ SHM, it is crucial to evaluate the capabilities of the sensing device when embedded into a composite structure. An experimental study of how the sensor is affected by the embedment process into a glass fiber-reinforced composite has been conducted. A series of devices with and without ML were embedded within a composite laminate, and the signal responses were collected under different conditions. We also demonstrated a successful encapsulation process in order for the device to withstand the composite manufacturing conditions. The results show that the sensor exhibits distinct signals when subjected to different load conditions and can be used for the in-situ SHM of advanced composite structures.

**Keywords:** structural health monitoring; mechanoluminescence; sensor; perovskite; composite material

## 1. Introduction

Composite materials have been attracting a lot of attention in industrial fields such as aeronautics, astronautics and automotive due to their improved strength-to-weight ratio and resistance to corrosion and fatigue [1]. Previous studies have demonstrated that the frequent exposure of composite structures to harsh conditions can compromise the structural integrity of the material [2–5]. Thus, there is a great interest in monitoring the health conditions of these structures. The structural health monitoring (SHM) system refers to techniques to track and evaluate the conditions of the structure over time using sensors and data analysis [6,7]. A lot of effort has been made in the development of efficient and reliable methods for the real-time monitoring of the health of structures for prolonged service. Mechanoluminescence (ML)-based sensors have been developed for damage sensing in multifunctional composite materials [8–14]. ML is the emission of light as a response to mechanical actions on a material [15]. ML can be triggered by pressure, crushing, impact load or wind action [8,11]. These materials can have many applications in stress sensing, dynamic pressure mapping, light sources or the detection of electric and magnetic fields [15,16]. In addition, ML materials can also be useful in determining crack propagation and stress distribution [6,8,10–12]. ML-based sensors have many advantages, such as simple device architecture, in-situ and self-power

sensing and robustness over the conventional sensing technologies used in SHM, such as piezoelectric devices [17–20]. Recently, Shohag et al. demonstrated a flexible, self-powered ML pressure sensor by integrating zinc sulfide:copper (ZnS:Cu) embedded in polydimethylsiloxane (PDMS) and a perovskite light-absorbing layer [8,17]. The light emitted by the ML layer is collected by the perovskite layer, which then converts light photons into an electrical current, avoiding the need for expensive equipment such as charge-coupled device (CCD) cameras and photomultipliers to collect ML emissions. Organic-inorganic perovskites offer a large light absorption coefficient, high and balanced charge carrier mobility, long carrier diffusion length, and other properties that make them attractive light-absorbing materials for photodetectors [21–25]. The ML-perovskite pressure sensor exhibits the potential for SHM applications [17]; however, the performance of the device remains relatively unexplored when embedded into a composite structure. Embedding the ML-perovskite sensor into composites structures could be an effective method for real-time and continuous SHM. Moreover, investigating the behavior of the device under embedment in a composite system is fundamental for future applications in SHM.

In this work, we assessed how the embedment process could affect the performance of the ML-perovskite sensor. The sensor was fabricated using a simplified structure, consisting of a planar hole-transporting layer-free structure of ZnS:Cu/polydimethylsiloxane(PDMS)/indium doped tin oxide (ITO)-Polyethylene terephthalate (PET)/tin (IV) oxide (SnO<sub>2</sub>)/perovskite/Au. It is worth mentioning that the performance of perovskite devices is known to be highly susceptible to degradation when exposed to ambient conditions [26]. Consequently, it is necessary to develop an encapsulation to protect the perovskite layer from rapid degradation and withstand the embedment process. It was observed that without encapsulation, the perovskite film could not survive the embedment, degrading when in contact with a resin matrix [27,28]. We developed a successful encapsulation process using a well-known commercial encapsulant, ethylene-vinyl acetate (EVA) and the embedment of this sensing device into a glass fiber-reinforced composite material. This work shows that the study of the ML-perovskite sensor's performance after embedment into a composite material creates new opportunities for future in-situ sensing based on mechanoluminescent sensor systems for SHM.

## 2. Materials and Methods

### 2.1. Materials and Reagent

Methylammonium Iodide (CH<sub>3</sub>NH<sub>3</sub>I),  $\gamma$ -butyrolactone ( $\gamma$ -GBL), N-methyl-2-pyrrolidone (NMP) and diethyl Ether (DEE) were purchased from Sigma–Aldrich. Lead iodide (PbI<sub>2</sub>) was purchased from Acros Organics. Lead bromide (PbBr<sub>2</sub>) and SnO<sub>2</sub> colloid precursor (15% in H<sub>2</sub>O colloidal dispersion) were purchased by Alfa Aesar. ZnS:Cu, GL29/B-C1, was purchased from Phosphor Technologies.

### 2.2. Device Fabrication

The device fabrication followed the same procedures described in our previously reported work [17]. Essentially, PET/ITO substrates were cut and patterned by etching with hydrochloric acid (HCl) and zinc (Zn) powder. The substrates were cleaned consecutively with Hellmanex detergent, nano pure water, acetone and isopropanol in a sonication bath. The PET substrates were treated with oxygen plasma for 5 min before the deposition of an electron transport layer (ETL) and perovskite. The colloidal SnO<sub>2</sub> precursor was diluted with deionized water to a 1:6 volume ratio. The ETL layer was prepared by spin-coating the solution at 3000 rpm for 30 s. The samples were annealed at 120 °C for 80 min in ambient conditions. The perovskite precursor solution was prepared by mixing 380 mg of CH<sub>3</sub>NH<sub>3</sub>I, 91.8 mg of PbBr<sub>2</sub> and 826.2 mg of PbI<sub>2</sub> into a solution of 1 mL of NMP and 0.2 mL of  $\gamma$ -GBL. The solution was left stirring on a hot plate at 70 °C overnight. Before deposition, the solution was heated on a hot plate at 70 °C for 30 min. The light-absorbing MAPb(Br<sub>0.1</sub>I<sub>0.9</sub>)<sub>3</sub> perovskite thin films were coated using a one-step deposition method and antisolvent bath method. The perovskite solution was spin-coated at 900 rpm for 3 s followed by 4500 rpm for 30 s. The substrates were dipped into DEE for 2 min and then annealed at 70 °C for 5 min followed by 130 °C for 15 min. Au electrode back

contacts were deposited on top of the perovskite via thermal evaporation. ZnS:Cu crystals, PDMS base and curing agent were mixed to a 20:10:1 weight ratio, respectively, using a planetary centrifugal mixer. The ZnS:Cu-PDMS blend was spin-coated on the opposite side of the PET substrate. The thin film was then heated until a complete cure was obtained. The encapsulation process was conducted in the following order: first, a slightly larger PET substrate was placed underneath the ML-perovskite device; then, an EVA sheet was placed on the top layer and used as an encapsulant. The device was further sealed using polyimide tape and laminated.

### 2.3. Material and Device Characterization

The absorption UV-Vis spectrum was collected using an UV-Vis spectrophotometer (Cary 5000, Agilent, Santa Clara, CA, USA). Scanning electron microscopy (SEM) images were collected by a high-resolution field emission scanning electron microscope (FESEM, JEOL 7401F, Tokyo, Japan). The current-voltage (*I-V*) measurements were obtained using a Keithley 2400 (Cleveland, OH, USA) source measure unit (Tektronix, Beaverton, OR, USA). The photovoltage-time measurements were collected using an NI-6210 data acquisition device and a Hamamatsu C7319 amplifier unit. An automated impact hammer equipment (AS-1220, Alta Solutions, San Diego, CA, USA) was used for the impact test.

## 3. Results and Discussion

### 3.1. Device Architecture

Figure 1 shows a schematic representation of the sensor device. The ML-perovskite sensor was fabricated using a simple planar structure consisting of ZnS:Cu-PDMS/ITO-PET/SnO<sub>2</sub>/perovskite/Au. Several robust and stable metal oxide-based ETLs have been used in the fabrication of vertical structure photodetectors. Among the metal oxides, titanium oxide (TiO<sub>2</sub>) is the most commonly used material. However, it requires high temperature (>450 °C) annealing to form a high-quality compact TiO<sub>2</sub> thin film, which is unattainable for applications in flexible substrates [29]. We introduced low-temperature processed SnO<sub>2</sub> as an alternative ETL, which is suitable for ITO-coated PET substrates with a maximum operating temperature of 120 °C [30–32]. It is worth mentioning that a vertical HTL-free architecture was adopted for the fabrication of the ML-perovskite pressure sensor to simplify the device architecture and reduce the fabrication cost. Although the utilization of HTL in perovskite photodetectors have been demonstrated to be effective in increasing the photodetector performance, most HTL materials, such as 2,2',7,7'-Tetrakis[N, N-di(4-Methoxyphenyl) Amino]-9,9'-spirobifluorene (Spiro-OMETAD), are expensive, which significantly increases the fabrication costs of the device [33–35]. The device fabrication was completed by thermal evaporation of the Au electrode on the perovskite layer [36–38]. In this structure, the electrical signal output is produced when the incident photons are absorbed by the perovskite layer, in which electron-hole pairs are produced. The holes are transported from the perovskite layer to the Au electrode, while the electrons are extracted by the SnO<sub>2</sub> layer.

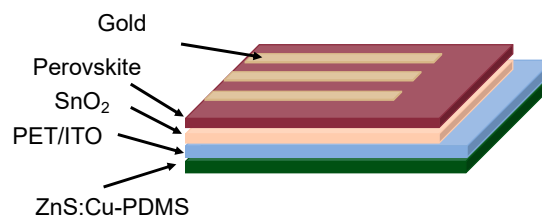


**Figure 1.** Schematics of the sensor device.

We conducted an investigation to assess the feasibility of embedding the ML-perovskite sensor into a composite. Our studies showed that the device could not survive the embedment process without any type of encapsulation. Immediately after contact with the matrix, the device (Figure 2a) was found

to show a degradation of the perovskite film (Figure 2b). After curing the resin, the perovskite layer completely deteriorated. Therefore, a robust and reliable encapsulation system for the device needs to be developed in order to successfully embed the ML-perovskite sensor into a composite structure.

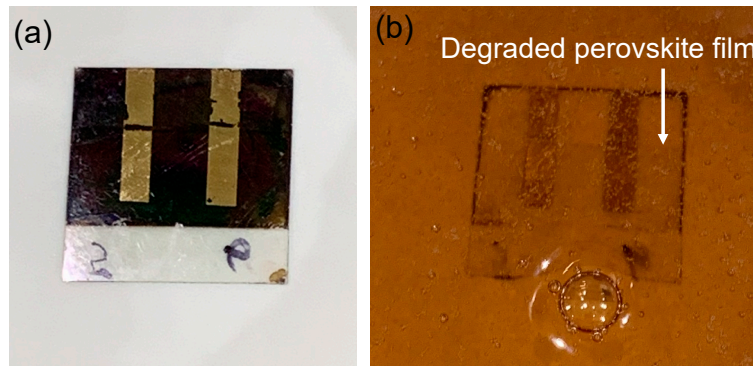


Figure 2. Photographs of the device (a) before and (b) after contact with vinyl-ester resin.

Figure 3a shows the schematics of the encapsulated device, and Figure 3b,c shows the final device. Glass fiber-woven reinforcement was chosen for two main reasons: (i) the transparency of the final composite allows the conditions of the device to be followed after the manufacturing process; (ii) the nonconductive characteristics of glass fibers prevent any electric interference between the fibers and the sensor. Figure 4 depicts the sensor embedment process in the glass fiber composite.

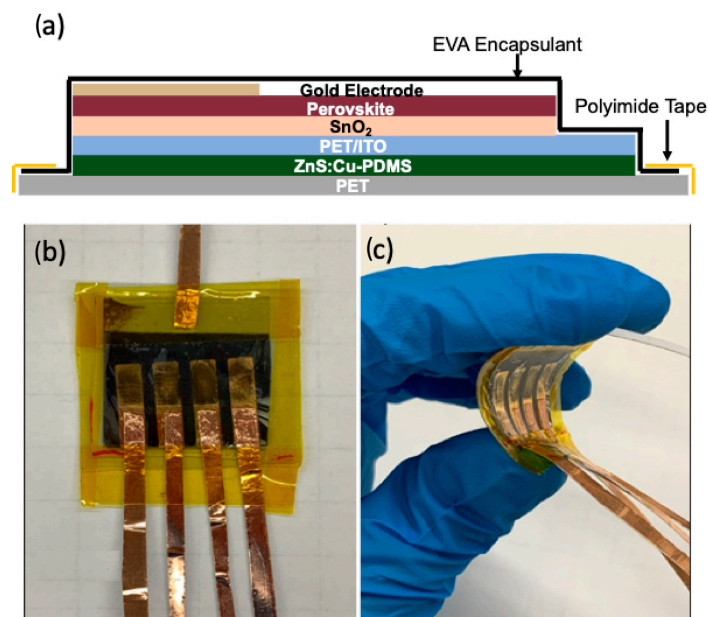


Figure 3. (a) Schematic of the encapsulated device; (b) top and (c) side view of the device.

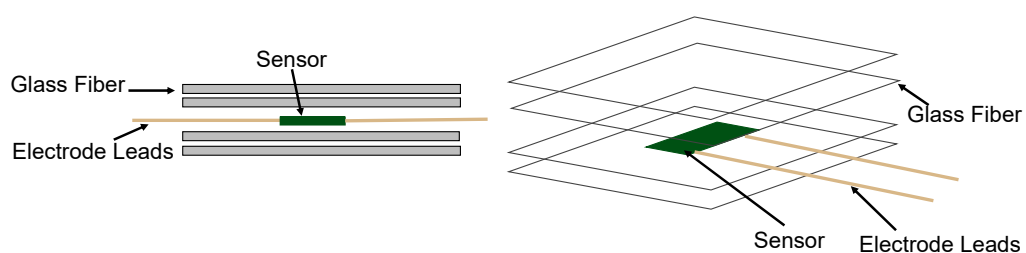
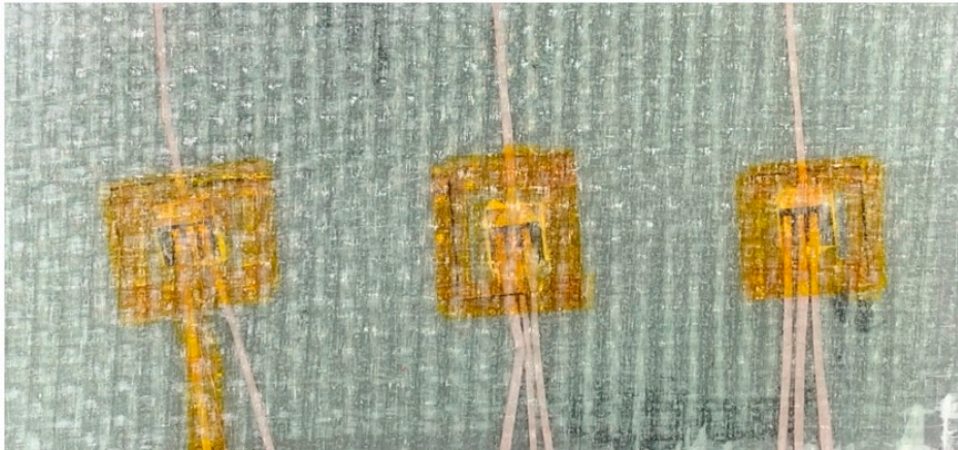


Figure 4. Schematics of the sensor embedment in the glass fiber composite.

The sensors were placed between four plies of glass fiber cloth-woven, as shown in Figure 5. A traditional vacuum-assisted resin transfer molding (VARTM) infusion was used, and vinyl-ester resin was used as a matrix. VARTM is a common out-of-autoclave manufacturing technique that is utilized in several industries [39]. The process has a relatively low-cost method and can be used to fabricate high-quality composite parts. Next, we assessed the performance behavior of the embedded sensor systems, which will be discussed below.



**Figure 5.** Embedded sensor in glass fiber-reinforced composite panel.

### 3.2. Device Characterization and Embedment

Figure 6a shows the UV-vis absorption spectrum of the  $\text{MAPb}(\text{Br}_{0.1}\text{I}_{0.9})_3$  film on the PET substrate and the ML emission of ZnS:Cu. The optical band gap ( $E_g$ ) of the  $\text{MAPb}(\text{Br}_{0.1}\text{I}_{0.9})_3$  perovskite is 1.64 eV, calculated from the Tauc plot, which is lower than the ML light emission  $E_g$  from ZnS:Cu (2.28 eV) [40]. Consequently, the ML emissions from ZnS:Cu can be fully absorbed by the perovskite material. The light emitted by the ZnS:Cu/PDMS layer as a result of the applied pressure or strain is responsible for exciting the perovskite layer, generating free electrons and hole pairs in the material, which are then transported to the cathode (ITO) and anode (Au), respectively. It has been previously reported that the ZnS:Cu/PDMS composite emits green light when stretched. The green ML emission was attributed to the deformation of the ZnS:Cu and frictional interactions between the ZnS:Cu and the PDMS [18,41,42]. The performance of the sensor is fundamentally dependent on the quality of the perovskite film. Figure 6b shows the SEM image of the high-quality uniform perovskite film, confirming the lack of pinholes and full crystallization of the material, which is beneficial for efficient light absorption and transport of photogenerated charge carriers within the bulk of the perovskite film. It is important to note that, in the absence of HTL the performance of the device is typically lower when compared with similar architectures with HTL. The choice of not including HTL is due to the fact that the development of a cheaper and easier to manufacture sensor was prioritized in this article. Etgar et al. reported that eliminating HTM in a solar cell structure prevented oxidation, reduced costs and provided better stability and consistent results [43]. It can be observed in Figure 6c that the device showed a stable and reproducible behavior when subjected to dark and light illumination, indicating that it could be used for sensing applications. Figure 6d shows the  $I$ - $V$  curves of the device under dark conditions before and after the embedment into a composite structure. After the embedment, the sensor remained functional, proving that the encapsulation process was successful. We also observed that the encapsulation or the embedment process affected the sensor electrical properties due to the noticeable differences in the dark  $I$ - $V$  curves. Notably, the dark current value dramatically decreased after encapsulation, as shown in Figure 6d. The underlying mechanism related to the decreased dark current is currently under investigation, and further work is in progress in order to gain a better understanding of the effects of encapsulation and embedment on the  $I$ - $V$  curve.

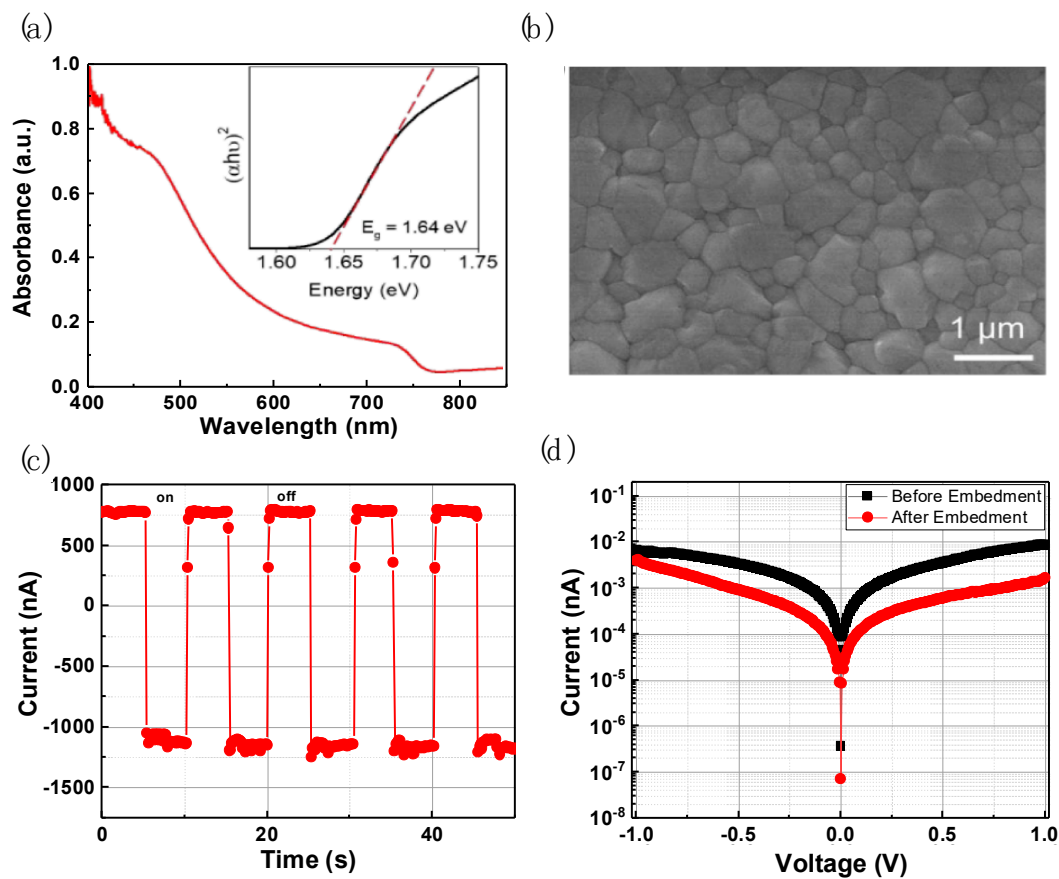


**Figure 6.** (a) UV-vis absorption spectrum [17]. (b) SEM image of the  $\text{MAPb}(\text{Br}_{0.1}\text{I}_{0.9})_3$  perovskite film [17]. (c) On-off cycles of the perovskite photodetector under white light. (d) I-V characteristics of the devices in the dark.

### 3.3. Sensor Response with Applied Pressure and Performance

The primary objective of this work was to analyze the performance and feasibility of the ML-perovskite sensor after embedment in a composite structure. An extensive and detailed characterization of the sensor response under various conditions has been previously reported [17].

A simple tapping test was conducted to verify the response of the sensor to applied pressure. Figure 7a shows the schematic representation of the experimental setup for the sensor's response upon finger tapping. The pressure was applied to the sensor several times and the tests were performed in ambient conditions (21 °C, 71% RH) and with no bias voltage. For a more standardized experimental procedure, automated impact hammer equipment was used. In total, 12 impacts with different magnitudes were executed on the composite panel, with a 2 s interval between the impacts. Figure 7b shows the impact hammer test result. The applied impact pressure varied from 100 kPa to 200 kPa.

The response of the sensor during the tapping test can be seen in Figure 8a, where  $\Delta I$  represents the change in current, and  $I_0$  represents the baseline current. The response signal of the sensor showed a similar pattern to triboelectric nanogenerator (TENG)-based sensors [44,45], resulting in positive and negative signals after contact with the sensor. It is likely that the ML-perovskite sensor is also influenced by triboelectric mechanisms from the friction contact between its layers. It is known that PDMS and ZnS:Cu can be used to fabricate a TENG sensor [44]. More thorough research needs to be conducted to investigate how this mechanism affects the functionalities of the ML-perovskite sensor. Table 1 shows a comparison of the performance characteristics of different types of sensing devices [17]. As can be seen, the ML-perovskite pressure sensor does not require any power at the sensing location,

which is advantageous for SHM applications. The sensitivity of the ML-perovskite sensor is impressive and comparable to other sensing devices summarized in Table 1.

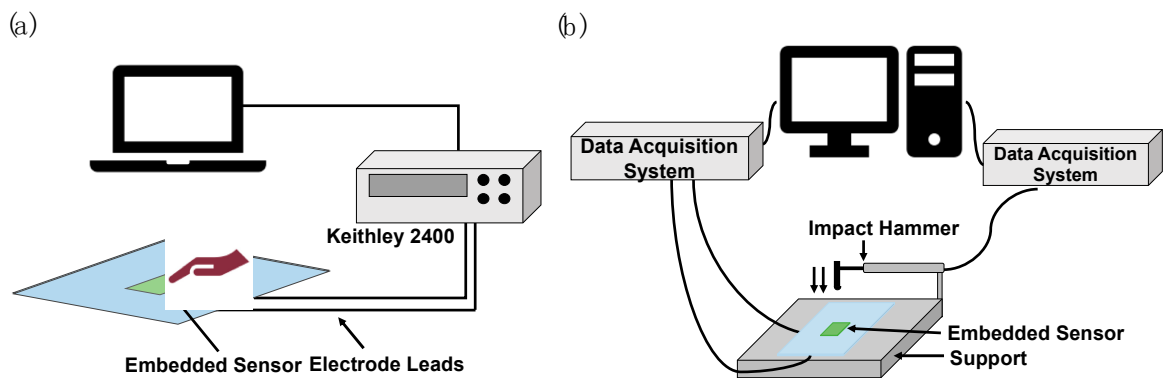


Figure 7. Schematics of the (a) tapping and (b) impact hammer experiment.

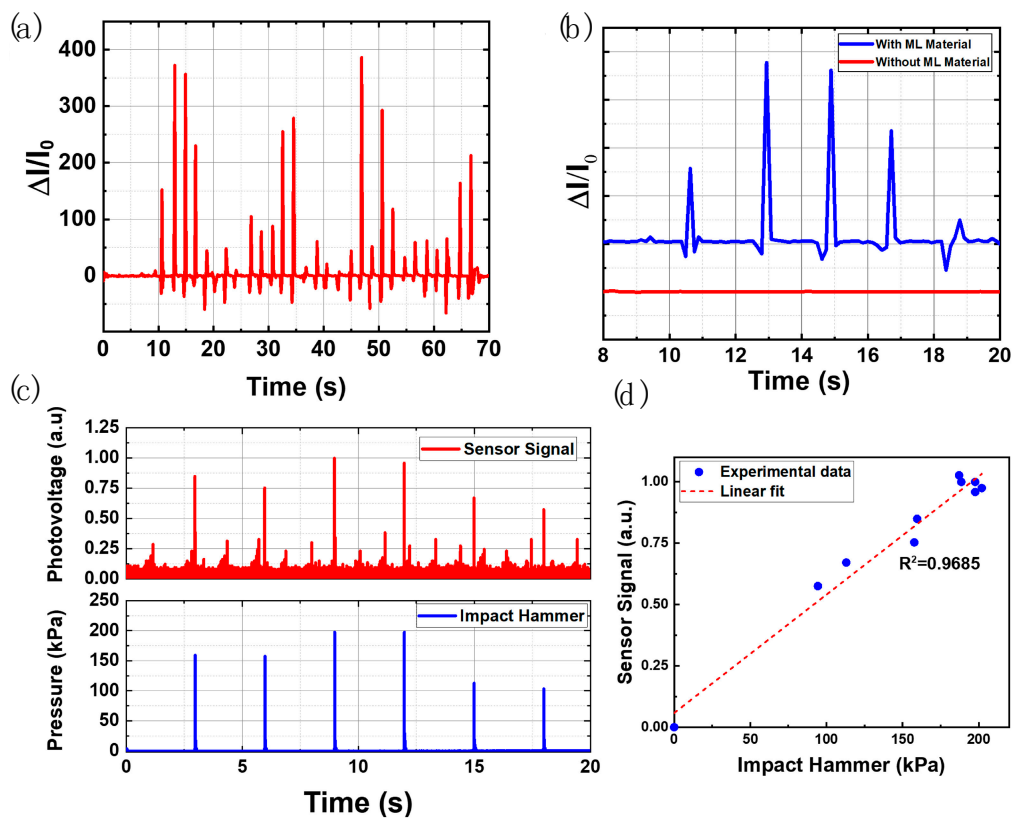


Figure 8. (a) Sensor response from the tapping test. (b) Comparison between the response signals from the sensor with ML material (blue) and without ML material (red). (c) Sensor response from the hammer impact test. (d) Correlation between the impact hammer strikes and the sensor signal.

**Table 1.** Comparison of the performance parameters of different types of sensors.

Sensor Type	Materials	Sensitivity/Min. Pressure	Power Consumption/Operating Voltage	Ref.
Mechanoluminescence/Perovskite	ZnS:Cu-PDMS/Perovskite	0.095 kPa <sup>-1</sup>	Self-powered	[17]
Mechanoluminescence	ZnS:Mn	0.7 cps kPa <sup>-1</sup> (0.6–10 Mpa) 2.2 cps kPa <sup>-1</sup> (10–50 Mpa)	Self-powered	[46]
Transistor/Mechanoluminescence	MoS2 FET/PDMS/ZnS:Cu	1.8 Mpa <sup>-1</sup> (<500 kPa) 0.045 Mpa <sup>-1</sup> (>500 kPa)	-	[47]
Capacitance/Transistor	PDMS	8.4 kPa <sup>-1</sup>	<1 mW	[48]
Capacitance	Microstructured PDMS	<10 kPa	80 V/0.75 mWcm <sup>-2</sup>	[49]
Resistance	Au Nanowires	>1.14 kPa <sup>-1</sup> /13 Pa	<30 uW	[50]
Resistance	PDMS/Pt-coated polyurethane acrylate/PDMS	3 Pa	-	[51]
Resistance	Nanofibers (carbon nanotubes and graphene)	1 kPa	-	[52]
Piezoresistance	PDMS micro-pyramid array/Pt-coated interlocking nanofibers	4.88 kPa <sup>-1</sup>	0.2 V	[53]
Piezoresistance	Elastic microstructured conducting polymer/Hollow-sphere structures of polypyrrole (Ppy)	133.1 kPa <sup>-1</sup> ( <i>p</i> < 30 kPa) 0.4 kPa <sup>-1</sup> ( <i>p</i> > 1 kPa)	-	[54]
Piezoresistance	Graphene-polyurethane sponge	0.03–0.26 kPa <sup>-1</sup>	<1 V/4 mWcm <sup>-2</sup>	[55]
Piezoresistance	SWNT/PDMS	1.8 kPa <sup>-1</sup>	2 V/0.007 mWcm <sup>-2</sup>	[56]

Furthermore, to confirm that the ML material was responsible for the signal responses of the device, a perovskite photodetector was embedded without an ML layer. All other processes were kept constant. Interestingly, without the ML material, no noticeable light emission occurred from the mechanical impact on the composite. As a result, no evident signals were observed (Figure 8b). It is possible to affirm that the light harvested by the perovskite came from the ML layer. Therefore, the addition of an ML material is fundamental to the performance of the sensor. Figure 8c shows the sensor response for the impact hammer test. The applied impact pressure varied from 100 kPa to 200 kPa, and the sensor generated distinct and consistent signals for the impacts, which demonstrated the sensor's viability for SHM applications in composite structures. When the most considerable impacts were taken into consideration, the impact strikes and the sensor signal were highly correlated, as shown in Figure 8d.

#### 4. Conclusions

In summary, this article investigated how the performance of the ML-perovskite device was affected by embedment in a glass fiber-reinforced composite. The embedment process was shown to be detrimental for the sensor, and an encapsulation process was necessary for the device to withstand the composite manufacturing process. The adoption of a simpler and cheaper HTL-free architecture was confirmed to be feasible for damage-sensing applications. However, the addition of HTL would increase the signal-to-noise ratio and the overall performance of the device. The sensor showed well-defined signals when subjected to different conditions. It was demonstrated that the ML layer was responsible

for the distinct response output of the sensor. The sensor did not require supplementary power to function, providing a great advantage over traditional sensors. To conclude, the ML-perovskite sensor can be embedded in an advanced composite material for in-situ SHM applications. The sensor presents an excellent potential for developing low-cost damage sensor devices for the SHM of smart composite materials. Future work is in progress to investigate the performance of the sensor under different conditions, such as thermal cycling and high-humidity environments.

**Author Contributions:** Conceptualization, L.B.C. and V.O.E.; methodology, L.B.C., V.O.E., C.I.; validation, L.B.C. and V.O.E.; formal analysis, V.O.E.; investigation, L.B.C., C.I., and V.O.E.; resources, O.I.O.; data curation, L.B.C. and V.O.E.; writing—original draft preparation, L.B.C.; writing—review and editing, V.O.E. and O.I.O.; visualization, V.O.E.; supervision, V.O.E. and O.I.O.; project administration, O.I.O.; funding acquisition, O.I.O. All authors have read and agreed to the published version of the manuscript.

**Funding:** The funding for this work was provided by the NSF award nos. 1359235 and NSF/DMR-1644779.

**Acknowledgments:** The authors thank Lance Cooley and Wenura K. Withanage from the Applied Superconductivity Center, National High Magnetic Field Laboratory, for performing the thermal evaporation of the gold electrodes.

**Conflicts of Interest:** The authors declare no conflict of interest.

## References

1. Bunsell, A.R.; Renard, J. *Fundamentals of Fibre Reinforced Composite Materials*, 1st ed.; CRC Press: Boca Raton, FL, USA, 2005; ISBN 978-0-7503-0689-8.
2. Ou, J.; Li, H. Structural health monitoring in mainland China: Review and future trends. *Struct. Health Monit.* **2010**, *9*, 219–231. [[CrossRef](#)]
3. Hsieh, K.H.; Halling, M.W.; Barr, P.J. Overview of vibrational structural health monitoring with representative case studies. *J. Bridge Eng.* **2006**, *11*, 707–715. [[CrossRef](#)]
4. Boller, C. Next generation structural health monitoring and its integration into aircraft design. *Int. J. Syst. Sci.* **2000**, *31*, 1333–1349. [[CrossRef](#)]
5. Baker, W.; McKenzie, I.; Jones, R. Development of life extension strategies for Australian military aircraft, using structural health monitoring of composite repairs and joints. *Compos. Struct.* **2004**, *66*, 133–143. [[CrossRef](#)]
6. Farrar, C.R.; Worden, K. An introduction to structural health monitoring. *Philos. Trans. R. Soc. A Math. Phys. Eng. Sci.* **2007**, *365*, 303–315. [[CrossRef](#)]
7. Daerefa-a Mitsheal, A.; Diogo, M.; Opukuro, D.-W.; George, H. A review of structural health monitoring techniques as applied to composite structures. *Struct. Durab. Health Monit.* **2017**, *11*, 91–147. [[CrossRef](#)]
8. Shohag, M.A.; Adams, G.R.; Eze, V.O.; Ichite, T.; Carani, L.B.; Okoli, O. Mechanoluminescent-Perovskite pressure sensor for structural health monitoring. In Proceedings of the Structural Health Monitoring, Santa Clara, CA, USA, 10–12 September 2019.
9. Jeong, S.M.; Song, S.; Seo, H.-J.; Choi, W.M.; Hwang, S.-H.; Lee, S.G.; Lim, S.K. Battery-Free, human-motion-powered light-emitting fabric: Mechanoluminescent textile. *Adv. Sustain. Syst.* **2017**, *1*, 1700126. [[CrossRef](#)]
10. Jeong, S.M.; Song, S.; Joo, K.-I.; Kim, J.; Hwang, S.-H.; Jeong, J.; Kim, H. Bright, wind-driven white mechanoluminescence from zinc sulphide microparticles embedded in a polydimethylsiloxane elastomer. *Energy Environ. Sci.* **2014**, *7*, 3338–3346. [[CrossRef](#)]
11. Jeong, S.M.; Song, S.; Lee, S.-K.; Ha, N.Y. Color Manipulation of mechanoluminescence from stress-activated composite films. *Adv. Mater.* **2013**, *25*, 6194–6200. [[CrossRef](#)]
12. Olawale, D.O.; Sullivan, G.; Dickens, T.; Tsalickis, S.; Okoli, O.I.; Sobanjo, J.O.; Wang, B. Development of a triboluminescence-based sensor system for concrete structures. *Struct. Health Monit.* **2012**, *11*, 139–147. [[CrossRef](#)]
13. Moon Jeong, S.; Song, S.; Lee, S.-K.; Choi, B. Mechanically driven light-generator with high durability. *Appl. Phys. Lett.* **2013**, *102*, 051110. [[CrossRef](#)]

14. Shohag, M.A.; Josh, K.; Ndebele, T.; Pollard, M.; Tran, S.; Braga Carani, L.; Dickens, T.; Okoli, O. Active sensors for load and damage monitoring in wind turbine blade: A hybrid manufacturing technique. In Proceedings of the 9th European Workshop on Structural Health Monitoring (EWSHM 2018), Manchester, UK, 10–13 July 2018.
15. Feng, A.; Smet, P.F. A Review of mechanoluminescence in inorganic solids: Compounds, mechanisms, models and applications. *Materials* **2018**, *11*, 484. [[CrossRef](#)]
16. Shohag, M.A.S.; Jiang, Z.; Hammel, E.C.; Braga Carani, L.; Olawale, D.O.; Dickens, T.J.; Wang, H.; Okoli, O.I. Development of friction-induced triboluminescent sensor for load monitoring. *J. Intell. Mater. Syst. Struct.* **2018**, *29*, 883–895. [[CrossRef](#)]
17. Shohag, M.A.S.; Eze, V.O.; Braga Carani, L.; Okoli, O.I. Fully Integrated Mechanoluminescent Devices with Nanometer-Thick Perovskite Film as Self-Powered Flexible Sensor for Dynamic Pressure Sensing. *ACS Appl. Nano Mater.* **2020**. [[CrossRef](#)]
18. Chandra, B.P.; Chandra, V.K.; Jha, P. Microscopic theory of elastico-mechanoluminescent smart materials. *Appl. Phys. Lett.* **2014**, *104*, 031102. [[CrossRef](#)]
19. Timilsina, S.; Kim, J.S.; Kim, J.; Kim, G.-W. Review of state-of-the-art sensor applications using mechanoluminescence microparticles. *Int. J. Precis. Eng. Manuf.* **2016**, *17*, 1237–1247. [[CrossRef](#)]
20. Olawale, D.O.; Dickens, T.; Sullivan, W.G.; Okoli, O.I.; Sobanjo, J.O.; Wang, B. Progress in triboluminescence-based smart optical sensor system. *J. Lumin.* **2011**, *131*, 1407–1418. [[CrossRef](#)]
21. Saparov, B.; Mitzi, D.B. Organic–inorganic perovskites: Structural versatility for functional materials design. *Chem. Rev.* **2016**, *116*, 4558–4596. [[CrossRef](#)]
22. Brenner, T.M.; Egger, D.A.; Kronik, L.; Hodes, G.; Cahen, D. Hybrid organic–Inorganic perovskites: Low-cost semiconductors with intriguing charge-transport properties. *Nat. Rev. Mater.* **2016**, *1*, 15007. [[CrossRef](#)]
23. Mitzi, D.B. Synthesis, structure, and properties of organic-inorganic perovskites and related materials. In *Progress in Inorganic Chemistry*; Karlin, K.D., Ed.; John Wiley & Sons, Inc.: Hoboken, NJ, USA, 2007; pp. 1–121. ISBN 978-0-470-16649-9.
24. Eze, V.O.; Adams, G.R.; Braga Carani, L.; Simpson, R.J.; Okoli, O.I. Enhanced inorganic cspbibr<sub>2</sub> perovskite film for a sensitive and rapid response self-powered photodetector. *J. Phys. Chem. C* **2020**, *124*, 20643–20653. [[CrossRef](#)]
25. Adams, G.R.; Eze, V.O.; Carani, L.B.; Pino, A.; Jolowsky, C.; Okoli, O.I. Synergistic effect of the anti-solvent bath method and improved annealing conditions for high-quality triple cation perovskite thin films. *RSC Adv.* **2020**, *10*, 18139–18146. [[CrossRef](#)]
26. Weerasinghe, H.C.; Dkhissi, Y.; Scully, A.D.; Caruso, R.A.; Cheng, Y.-B. Encapsulation for improving the lifetime of flexible perovskite solar cells. *Nano Energy* **2015**, *18*, 118–125. [[CrossRef](#)]
27. Wong-Stringer, M.; Game, O.S.; Smith, J.A.; Routledge, T.J.; Alqurashy, B.A.; Freestone, B.G.; Parnell, A.J.; Vaenas, N.; Kumar, V.; Alawad, M.O.A.; et al. High-performance multilayer encapsulation for perovskite photovoltaics. *Adv. Energy Mater.* **2018**, *8*, 1801234. [[CrossRef](#)]
28. Barbé, J.; Pockett, A.; Stoichkov, V.; Hughes, D.; Lee, H.K.H.; Carnie, M.; Watson, T.; Tsoi, W.C. In situ investigation of perovskite solar cells' efficiency and stability in a mimic stratospheric environment for high-altitude pseudo-satellites. *J. Mater. Chem. C* **2020**, *8*, 1715–1721. [[CrossRef](#)]
29. Eze, V.O.; Seike, Y.; Mori, T. Efficient planar perovskite solar cells using solution-processed amorphous WO<sub>x</sub>/fullerene C 60 as electron extraction layers. *Org. Electron.* **2017**, *46*, 253–262. [[CrossRef](#)]
30. ITO-Coated PET Film. Available online: [https://www.thorlabs.com/newgrouppage9.cfm?objectgroup\\_id=9535](https://www.thorlabs.com/newgrouppage9.cfm?objectgroup_id=9535) (accessed on 15 December 2020).
31. Chen, Y.; Meng, Q.; Zhang, L.; Han, C.; Gao, H.; Zhang, Y.; Yan, H. SnO<sub>2</sub>-based electron transporting layer materials for perovskite solar cells: A review of recent progress. *J. Energy Chem.* **2019**, *35*, 144–167. [[CrossRef](#)]
32. Park, M.; Kim, J.-Y.; Son, H.J.; Lee, C.-H.; Jang, S.S.; Ko, M.J. Low-temperature solution-processed Li-doped SnO<sub>2</sub> as an effective electron transporting layer for high-performance flexible and wearable perovskite solar cells. *Nano Energy* **2016**, *26*, 208–215. [[CrossRef](#)]
33. Zhang, Z.; Zhang, W.; Jiang, Q.; Wei, Z.; Deng, M.; Chen, D.; Zhu, W.; Zhang, J.; You, H. Toward high-performance electron/hole-transporting-layer-free, self-powered cspbibr<sub>2</sub> photodetectors via interfacial engineering. *ACS Appl. Mater. Interfaces* **2020**, *12*, 6607–6614. [[CrossRef](#)]

34. Liu, X.; Liu, Z.; Li, J.; Tan, X.; Sun, B.; Fang, H.; Xi, S.; Shi, T.; Tang, Z.; Liao, G. Ultrafast, self-powered and charge-transport-layer-free photodetectors based on high-quality evaporated CsPbBr<sub>3</sub> perovskites for applications in optical communication. *J. Mater. Chem. C* **2020**, *8*, 3337–3350. [[CrossRef](#)]
35. Ma, Q.; Huang, S.; Wen, X.; Green, M.A.; Ho-Baillie, A.W.Y. Hole transport layer free inorganic CsPbBr<sub>2</sub> perovskite solar cell by dual source thermal evaporation. *Adv. Energy Mater.* **2016**, *6*, 1502202. [[CrossRef](#)]
36. Lin, S.; Yang, B.; Qiu, X.; Yan, J.; Shi, J.; Yuan, Y.; Tan, W.; Liu, X.; Huang, H.; Gao, Y.; et al. Efficient and stable planar hole-transport-material-free perovskite solar cells using low temperature processed SnO<sub>2</sub> as electron transport material. *Org. Electron.* **2018**, *53*, 235–241. [[CrossRef](#)]
37. Bhatt, P.; Pandey, K.; Yadav, P.; Tripathi, B.; Kanth P., C.; Pandey, M.K.; Kumar, M. Investigating the charge carrier transport within the hole-transport material free perovskite solar cell processed in ambient air. *Sol. Energy Mater. Sol. Cells* **2015**, *140*, 320–327. [[CrossRef](#)]
38. Etgar, L. Hole-transport material-free perovskite-based solar cells. *MRS Bull.* **2015**, *40*, 674–680. [[CrossRef](#)]
39. Ulven, C.; Vaidya, U.K.; Hosur, M.V. Effect of projectile shape during ballistic perforation of VARTM carbon/epoxy composite panels. *Compos. Struct.* **2003**, *61*, 143–150. [[CrossRef](#)]
40. Hoang, K.; Latouche, C.; Jobic, S. Defect energy levels and persistent luminescence in Cu-doped ZnS. *Comput. Mater. Sci.* **2019**, *163*, 63–67. [[CrossRef](#)]
41. Shin, S.W.; Oh, J.P.; Hong, C.W.; Kim, E.M.; Woo, J.J.; Heo, G.-S.; Kim, J.H. Origin of mechanoluminescence from Cu-doped ZnS particles embedded in an elastomer film and its application in flexible electro-mechanoluminescent lighting devices. *ACS Appl. Mater. Interfaces* **2016**, *8*, 1098–1103. [[CrossRef](#)]
42. Chandra, V.K.; Chandra, B.P.; Jha, P. Self-recovery of mechanoluminescence in ZnS:Cu and ZnS:Mn phosphors by trapping of drifting charge carriers. *Appl. Phys. Lett.* **2013**, *103*, 161113. [[CrossRef](#)]
43. Etgar, L.; Gao, P.; Xue, Z.; Peng, Q.; Chandiran, A.K.; Liu, B.; Nazeeruddin, M.K.; Grätzel, M. Mesoscopic CH<sub>3</sub> NH<sub>3</sub> PbI<sub>3</sub>/TiO<sub>2</sub> Heterojunction Solar Cells. *J. Am. Chem. Soc.* **2012**, *134*, 17396–17399. [[CrossRef](#)]
44. Park, H.-J.; Kim, S.; Lee, J.H.; Kim, H.T.; Seung, W.; Son, Y.; Kim, T.Y.; Khan, U.; Park, N.-M.; Kim, S.-W. Self-powered motion-driven triboelectric electroluminescence textile system. *ACS Appl. Mater. Interfaces* **2019**, *11*, 5200–5207. [[CrossRef](#)]
45. Wang, J.; Qian, S.; Yu, J.; Zhang, Q.; Yuan, Z.; Sang, S.; Zhou, X.; Sun, L. Flexible and wearable PDMS-based triboelectric nanogenerator for self-powered tactile sensing. *Nanomaterials* **2019**, *9*, 1304. [[CrossRef](#)]
46. Wang, X.; Zhang, H.; Yu, R.; Dong, L.; Peng, D.; Zhang, A.; Zhang, Y.; Liu, H.; Pan, C.; Wang, Z.L. Dynamic pressure mapping of personalized handwriting by a flexible sensor matrix based on the mechanoluminescence process. *Adv. Mater.* **2015**, *27*, 2324–2331. [[CrossRef](#)] [[PubMed](#)]
47. Jang, J.; Kim, H.; Ji, S.; Kim, H.J.; Kang, M.S.; Kim, T.S.; Won, J.; Lee, J.-H.; Cheon, J.; Kang, K.; et al. Mechanoluminescent, air-dielectric MoS<sub>2</sub> transistors as active-matrix pressure sensors for wide detection ranges from footsteps to cellular motions. *Nano Lett.* **2020**, *20*, 66–74. [[CrossRef](#)] [[PubMed](#)]
48. Schwartz, G.; Tee, B.C.-K.; Mei, J.; Appleton, A.L.; Kim, D.H.; Wang, H.; Bao, Z. Flexible polymer transistors with high pressure sensitivity for application in electronic skin and health monitoring. *Nat. Commun.* **2013**, *4*, 1859. [[CrossRef](#)]
49. Mannsfeld, S.C.B.; Tee, B.C.-K.; Stoltenberg, R.M.; Chen, C.V.H.-H.; Barman, S.; Muir, B.V.O.; Sokolov, A.N.; Reese, C.; Bao, Z. Highly sensitive flexible pressure sensors with microstructured rubber dielectric layers. *Nat. Mater.* **2010**, *9*, 859–864. [[CrossRef](#)]
50. Gong, S.; Schwalb, W.; Wang, Y.; Chen, Y.; Tang, Y.; Si, J.; Shirinzadeh, B.; Cheng, W. A wearable and highly sensitive pressure sensor with ultrathin gold nanowires. *Nat. Commun.* **2014**, *5*, 3132. [[CrossRef](#)]
51. Pang, C.; Lee, G.-Y.; Kim, T.; Kim, S.M.; Kim, H.N.; Ahn, S.-H.; Suh, K.-Y. A flexible and highly sensitive strain-gauge sensor using reversible interlocking of nanofibres. *Nat. Mater.* **2012**, *11*, 795–801. [[CrossRef](#)]
52. Lee, S.; Reuveny, A.; Reeder, J.; Lee, S.; Jin, H.; Liu, Q.; Yokota, T.; Sekitani, T.; Isoyama, T.; Abe, Y.; et al. A transparent bending-insensitive pressure sensor. *Nat. Nanotechnol.* **2016**, *11*, 472–478. [[CrossRef](#)]
53. Choong, C.-L.; Shim, M.-B.; Lee, B.-S.; Jeon, S.; Ko, D.-S.; Kang, T.-H.; Bae, J.; Lee, S.H.; Byun, K.-E.; Im, J.; et al. Highly stretchable resistive pressure sensors using a conductive elastomeric composite on a micropillar array. *Adv. Mater.* **2014**, *26*, 3451–3458. [[CrossRef](#)]
54. Pan, L.; Chortos, A.; Yu, G.; Wang, Y.; Isaacson, S.; Allen, R.; Shi, Y.; Dauskardt, R.; Bao, Z. An ultra-sensitive resistive pressure sensor based on hollow-sphere microstructure induced elasticity in conducting polymer film. *Nat. Commun.* **2014**, *5*, 3002. [[CrossRef](#)]

55. Yao, H.-B.; Ge, J.; Wang, C.-F.; Wang, X.; Hu, W.; Zheng, Z.-J.; Ni, Y.; Yu, S.-H. A Flexible and highly pressure-sensitive graphene-polyurethane sponge based on fractured microstructure design. *Adv. Mater.* **2013**, *25*, 6692–6698. [[CrossRef](#)]
56. Wang, X.; Gu, Y.; Xiong, Z.; Cui, Z.; Zhang, T. Silk-Molded flexible, ultrasensitive, and highly stable electronic skin for monitoring human physiological signals. *Adv. Mater.* **2014**, *26*, 1336–1342. [[CrossRef](#)]

**Publisher’s Note:** MDPI stays neutral with regard to jurisdictional claims in published maps and institutional affiliations.



© 2020 by the authors. Licensee MDPI, Basel, Switzerland. This article is an open access article distributed under the terms and conditions of the Creative Commons Attribution (CC BY) license (<http://creativecommons.org/licenses/by/4.0/>).